JOURNAL OF AIRCRAFT
Vol. 40, No. 1, January–February 2003

Validation of a Simulation Model for a Planetary Entry Capsule

Giorgio Guglieri* and Fulvia Quagliotti†
Politecnico di Torino, 10129 Turin, Italy

Subsonic static and oscillatory aerodynamic coefficients were measured at Politecnico di Torino for a planetary entry capsule model. The experimental data set was included in a mathematical model of payload-decelerator system, and the results of simulations were compared with flight-test data. The frequency-domain attitude response of the capsule was reproduced during the main parachutes' deployment, and discrepancies for the drogue opening phase were observed. The impact on simulations of atmospheric turbulence and asymmetries in the parachute suspension system was also considered. The results suggest that several factors may affect the fidelity of simulations such as correct modeling of suspension system geometry and flexibility, parachute aerodynamics, accuracy of payload inertial data, and accurate matching of real flight external perturbations. The effect of some design parameters on capsule attitude dynamics was evaluated. The artificial increase of capsule damping coefficients produced observable effects on attitude time histories for large perturbations of the aerodynamic derivatives only. The dynamic stability of the system is reduced for large increase of riser length and parachute added mass.

Nomenclature

C_{DP}	=	parachute drag coefficient, $D_P/q_\infty S_P$
C_l	=	rolling moment coefficient, $L/q_\infty Sd$
C_m	=	pitching moment coefficient, $M/q_\infty Sd$
C_n	=	yawing moment coefficient, $N/q_\infty Sd$
C_X	=	axial force coefficient, $X/q_\infty S$
C_Y	=	lateral force coefficient, $Y/q_\infty S$
C_Z	=	normal force coefficient, $Z/q_\infty S$
C^*_{iq}	=	damping derivative, $C_{iq} + C_{i\dot{\alpha}} = \partial C_i/\partial\hat{q} + \partial C_i/\partial\hat{\dot{\alpha}}$, where $i = X, Z, m$
D_P	=	parachute drag
d	=	reference length (capsule diameter)
F	=	elastic force
I_{ay}	=	added moment of inertia of the parachute
I_x, I_y, I_z, I_{xz}	=	mass moments of inertia
K	=	elastic constant
L	=	rolling moment
L_b	=	additional rolling moment due to bridles
l	=	length
M	=	pitching moment
m	=	mass
m_{ax}, m_{ay}	=	axial and transverse added masses of the parachute
N	=	yawing moment
N_b	=	additional yawing moment due to bridles
p, q, r	=	angular rates (capsule)
q_∞	=	dynamic pressure, $\rho V^2/2$
Re	=	Reynolds number, based on capsule diameter d
S	=	reference area, $\pi d^2/4$
S_P	=	parachute reference area
s, y, h	=	Earth-fixed axes
$[T_{BV}]$	=	rotation matrix from s, y, h to x_B, y_B, z_B; $f(\phi, \theta, \psi)$
$[T_{PV}]$	=	rotation matrix from s, y, h to x_P, y_P, z_P; $f(\phi_P, \theta_P, \psi_P)$
u, v, w	=	velocity components
V	=	capsule airspeed, $\sqrt{(u^2 + v^2 + w^2)}$
V_P	=	parachute airspeed, $\sqrt{(u_P^2 + v_P^2 + w_P^2)}$
X	=	axial force
x, z	=	auxiliary body-fixed longitudinal axes (origin at capsule theoretical apex)
x_B, y_B, z_B	=	body-fixed axes (origin at capsule c.g.)
x_P, y_P, z_P	=	body-fixed axes (origin at parachute c.g.)
Y	=	lateral force
Z	=	normal force
α, β	=	angle of attack and sideslip (capsule)
Δl	=	length increment
ϵ	=	strain, $\Delta l/l$
σ	=	total angle of attack (capsule)
$\bar{\sigma}$	=	measurement accuracy of wind-tunnel data
τ, χ	=	angular displacement of the riser with respect to s, y, h (see Fig. 1)
ϕ, θ, ψ	=	Euler angles
ϕ_a	=	aerodynamic roll angle (capsule)

Subscripts

b	=	bridle
CG	=	center of gravity (capsule)
CP	=	center of gravity (parachute)
g	=	gust
P	=	parachute
PA	=	parachute attach point
$P2$	=	point of confluence of riser and suspension lines
r	=	riser
s	=	suspension line
0	=	reference condition
1, 2, 3	=	vector components

Received 25 January 2002; revision received 12 September 2002; accepted for publication 13 September 2002.

*Assistant Professor, Dip. Ingegneria Aeronautica e Spaziale, Corso Duca degli Abruzzi 24; guglieri@polito.it. Senior Member AIAA.
†Associate Professor, Dip. Ingegneria Aeronautica e Spaziale, Corso Duca degli Abruzzi 24; quagliotti@polito.it. Senior Member AIAA.

Introduction

MOST of the research activity concerning nonlifting reentry configurations and the analysis of their decelerated reentry phase was performed during the early development of space missions. New research programs concerning capsule aerodynamics and flight dynamics have been recently carried out, due to the interest for applications such as planetary entry probes and crewed capsules.

The dynamic stability of blunt bodies such as capsule shapes and planetary entry probes has been shown to be poor in subsonic flight.[1] The near wake recirculation and the rear flowfield pattern are responsible for the unstable dynamic behavior as a consequence

of time lags in the wake[2] that provide a destabilizing driving force. It follows a difficult investigation of the dynamic characteristics of capsules. Numerical and experimental methods are still inadequate to predict accurately the complex aerodynamics of these vehicles, which generally exhibit an extended unsteady separated flow. A vehicle whose static stability appears acceptable from wind-tunnel experiments may have dynamic instabilities that can lead to divergence or unacceptable behavior in flight.

The retardation required to control the airspeed of the capsule during the terminal phase of the reentry may be provided by means of parachutes. A complete overview of parachute technology including aerodynamics and payload-decelerator dynamics is given in Ref. 3.

For many applications, parachute and capsule systems can be treated as a single rigid mass. This method is sufficient when only the trajectory of the payload must be simulated. However, two coupled masses must be taken into account when the relative motion of the two subsystems is of interest for a complete simulation of attitude dynamics. To predict the dynamic behavior of these complex systems, a parallel activity concerning the development of accurate mathematical models for the simulation of the terminal descent of a capsule decelerated by one or more parachutes was carried out.

A three-degree-of-freedom analysis is presented and validated in Ref. 4 giving the longitudinal motion of a typical vehicle during the recovery. The parachute and the payload are supposed to be rigid and interconnected by an elastic riser. Aerodynamic loads acting on the two subsystems are considered. Computer results showed good agreement with test results in terms of oscillation amplitude and frequency, riser force, and parachute wrapup about the vehicle for the simulation of a pad-abort situation.

The three-dimensional motion of a freely descending parachute is studied in Ref. 5 with a five-degree-of-freedom analysis. The roll motion is neglected. Exact expressions are given for the longitudinal and lateral small disturbance stability of the gliding motion of parachutes. The analysis confirms that large longitudinal disturbance of most parachutes will result in a large pitching motion, whereas a large lateral disturbance will usually cause a large angle vertical coning motion (coning mode). The longitudinal mode damps out very quickly in the stable case.

The three-dimensional motion of a nonrigid parachute and payload system is studied in Ref. 6. Both the parachute and the payload are assumed to have five degree of freedom. Roll about axis of symmetry is neglected. They are coupled together by a fixed length connector. The general nonlinear equations are linearized using the small perturbation theory. The evaluation of the stability of an unstable payload decelerated by a parachute is performed. The authors observed that increasing riser length and parachute weight promotes system instability.

A nine-degree-of-freedom computer program was developed in Ref. 7 for the simulation of the trajectory and the dynamic behavior of a rotating parachute system. An appropriate mathematical model of the joint between the load and the parachute was found to be necessary to predict the dynamic behavior of a rotating decelerated system.

A computer model based upon a six-degree-of-freedom analysis is described in Ref. 8 and compared with drop test data. The payload is rigidly connected, the aerodynamic forces on canopy and payload are determined by the instantaneous angle of attack of the oncoming airstream, and the apparent masses are constant, but they are dependent on the direction of the acceleration.

Full nonlinear equations of motion for the axisymmetric parachute have been obtained in Ref. 9. In particular, the correct form of the added mass tensor for a rigid axisymmetric parachute in ideal flow has been implemented in a six-degree-of-freedom computer model,[10] and the results indicate that added mass effects are significant. In particular, the component of added mass along the axis of symmetry has a strong effect on parachute dynamic stability. However, design and testing experience shows that dynamic stability of the parachute is a second-order design problem[3] for high-performance decelerators, which usually have both high static and dynamic stability due to the porosity of the canopy.

ESA was recently involved in the design of a reentry capsule that can return to Earth carrying payloads and/or crew. A technology demonstrator[11,12] has been developed: the Atmospheric Reentry Demonstrator (ARD). The design of the ARD is based on the geometry of the Apollo command module (ACM), and it is substantially a scaled version of the original Apollo capsule. The ARD is an uncrewed three-axis stabilized automatic vehicle that can be injected into a suborbital ballistic path. Atmospheric friction and a series of parachutes must slow it down before landing in the sea. Balloon flight tests were also performed to qualify the descent and recovery subsystem.[13] The complete ARD mission was successfully performed after the Ariane 503 flight (October 1998).

Attitude dynamics of the ARD was analyzed[11] by means of multibody dynamics. The simulation of a parachute inflation and descent phase was compared with flight-test data. Parachute loads and payload accelerations were correctly predicted, although some discrepancy was observed for attitude dynamics that are substantially affected by gusts and atmospheric turbulence. The accuracy of attitude simulations was also influenced by the uncertainty of available experimental data[14] concerning the aerodynamic damping coefficients $C_{iq} + C_{i\dot{\alpha}}$ of the capsule.

To provide a new accurate experimental data set of the ACM configuration, the static and dynamic stability characteristics of the capsule were evaluated at the von Kármán Institute (see Refs. 15 and 16) with a set of static and oscillatory wind-tunnel experiments at subsonic and transonic speeds. The wake behind the Apollo capsule was also analyzed, and the similarity of the model wake with the real ACM was verified.[16] These experiments confirmed that the dynamic stability of the ACM is compromised during the reentry phase by the unsteady interaction of the recirculating flow behind the capsule and the separated flow in the wake.

An experimental program[17] supported by the Italian Space Agency was also performed at Politecnico di Torino. Static and oscillatory data were measured for a reference model of ACM to extend the available experimental database for different testing conditions (Reynolds numbers, c.g. locations, and oscillation parameters). The longitudinal stability of the equivalent real capsule with and without decelerators was also investigated using a simplified model. An extended higher-order mathematical model has been now validated by comparing the results of simulations with flight-test data for the terminal reentry phase of the ARD mission.

Present Work

The objectives of this paper are 1) to include the experimental data set obtained at Politecnico di Torino for the ACM configuration in a mathematical model of payload-decelerator system, 2) to validate the system dynamic response with flight-test data, and 3) to evaluate the impact of some design parameters on capsule attitude dynamics.

Mathematical Model

The simulation algorithm performs the numerical integration of a system of first-order differential equations. The mathematical model of the decelerated capsule is based on the assumption that the payload and the parachute are rigid bodies connected by an elastic riser that is able to be stretched by the relative motion of the two components (Fig. 1). The layout in Fig. 1 is not scaled to the real case, and it is only introduced to define the geometry of the system. The equations for the dynamic equilibrium of the two bodies are integrated separately, and the joints in the system are supposed to be frictionless. The mass of the two subsystems is updated at each time step including the apparent mass of the decelerator, which is added to the physical mass for computing the inertial loads. No apparent mass effect is considered for the payload. The parachute is handled as a rigid body in the fully inflated configuration, neglecting the flexibility of the canopy and of the suspension lines. The relative displacement of payload and parachute produces an elongation of the riser and an elastic reaction F_r that is included in the equilibrium of the two subsystems. Hence, the dynamic response of the two masses is coupled because the decelerating forces generated by the parachute are transmitted to the capsule by means of the riser,

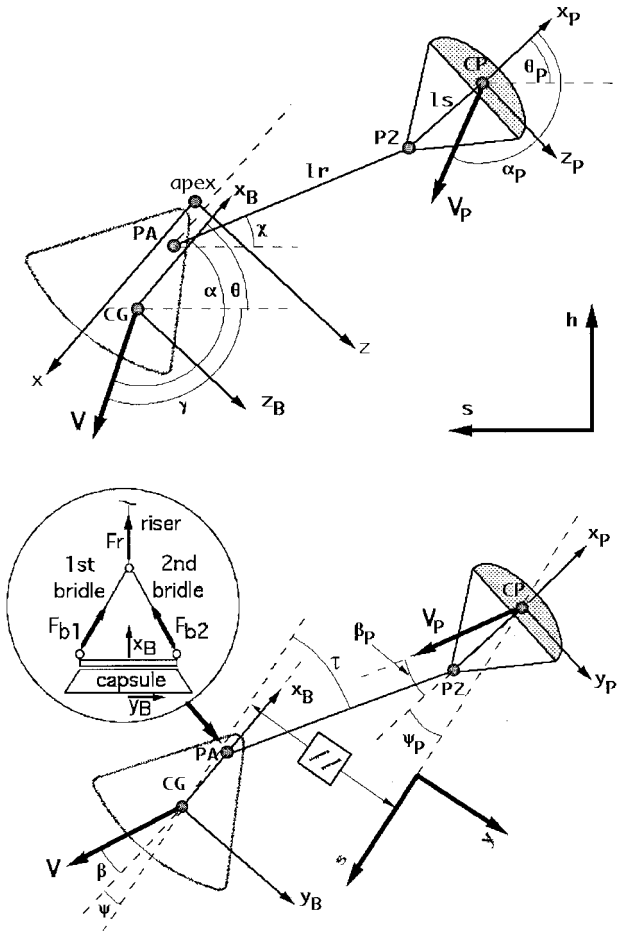

Fig. 1 Geometry of the system (longitudinal and lateral–directional plane).

connected to the attach point (PA). Meanwhile, the forces acting on the capsule (aerodynamic and inertial loads) are reduced in the confluence point $P2$ of the parachute.

The presence of the bridles, linked to the PA, is modeled by means of two separate elastic components (linear hard-stop devices), which are supposed to withstand the load F_r aligned with the riser. Their differential elongation generates two additional lateral–directional torque components acting on the payload: the rolling moment L_b and the yawing moment N_b.

The main aerodynamic load acting on the parachute is the drag $D_P = q_\infty C_{DP} S_P$ aligned with the local direction of the airspeed V_P. The effect of parachute angle of attack on canopy aerodynamic lift and drag is considered. An efficiency factor for body wake interaction is introduced as a multiplier of dynamic pressure at the canopy for the drogue parachute only. This last correction is based on matching of the capsule deceleration profile after parachute inflation. The geometry of the canopy is assumed axisymmetric. Clustered decelerators are treated as a single parachute with the same drag area $C_{DP} S_P$ and equivalent included mass of air.

The formulation adopted for the aerodynamic loads of the payload is based on the static and dynamic derivatives obtained during the wind-tunnel experiments performed at Politecnico di Torino.[17] The measurement accuracy for the static coefficient C_m is $\bar{\sigma} \approx \pm 0.1\%$ estimated over the full range, and $\bar{\sigma} \approx \pm 1\%$ for the longitudinal stability derivative $C_{mq} + C_{m\dot{\alpha}}$.

The aerodynamic reactions are obtained assuming that symmetry applies for the capsule, that is, the coefficients (Figs. 2 and 3) are interpolated after table look-up of the experimental data (incompressible flow is assumed) with respect to the total angle of attack $\sigma = \arctan\sqrt{(v^2 + w^2)/u^2}$ in the plane defined by the body axis x_B and the velocity vector $\boldsymbol{V}$.

The coefficients are combined in a mathematical formulation that is based on the superposition of steady-state aerodynamics and

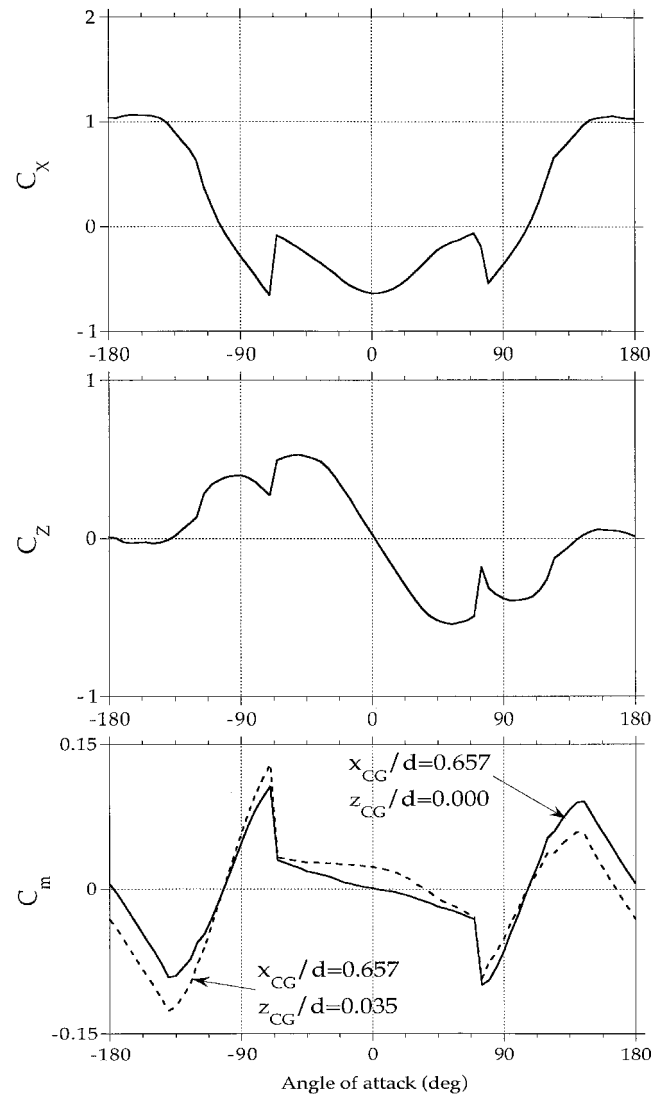

Fig. 2 Capsule static coefficients, $V = 30$ m/s and $Re = 6.23 \times 10^5$.

damping effects:

$$X = q_\infty S \cdot C_X(\sigma) + q_\infty S \cdot C^*_{Xq}(\sigma, x_{CG}, z_{CG} = 0) \cdot \dot{\sigma} d/\boldsymbol{V}$$

$$Z = q_\infty S \cdot C_Z(\sigma) + q_\infty S \cdot C^*_{Zq}(\sigma, x_{CG}, z_{CG} = 0) \cdot \dot{\sigma} d/\boldsymbol{V}$$

$$M = q_\infty Sd \cdot C_m(\sigma, x_{CG}, z_{CG} = 0) + q_\infty Sd \cdot C^*_{mq}(\sigma, x_{CG}, z_{CG} = 0) \cdot \dot{\sigma} d/\boldsymbol{V} \tag{1}$$

where the time derivative of σ is given by

$$\dot{\sigma} = \frac{uv\dot{v} + uw\dot{w} - (v^2 + w^2)\dot{u}}{\boldsymbol{V}^2 \cdot \sqrt{v^2 + w^2}} \tag{2}$$

Then, the aerodynamic roll angle $\phi_a = \arctan(v/w)$ is used to rotate the aerodynamic loads in the primary reference frame x_B, y_B, and z_B including the effect of capsule c.g. location.

The equations of motion for the vehicle (with respect to the body axes x_B, y_B, and z_B) are

$$\dot{u} = \frac{X + F_{r_1}}{m} - qw + vr - g\sin\theta$$

$$\dot{v} = \frac{Y + F_{r_2}}{m} - ru + pw + g\cos\theta\sin\phi$$

$$\dot{w} = \frac{Z + F_{r_3}}{m} - pv + qu + g\cos\theta\cos\phi$$

$$\dot{p} = \frac{I_{xz}\left[N + F_{r_2}(x_{\mathrm{CG}} - x_{\mathrm{PA}}) + N_b\right] + I_z\left[L + F_{r_2}(z_{\mathrm{CG}} - z_{\mathrm{PA}}) + L_b\right]}{I_x I_z - I_{xz}^2} + \frac{I_{xz}(I_x - I_y + I_z)pq - \left(I_z^2 - I_y I_z + I_{xz}^2\right)rq}{I_x I_z - I_{xz}^2}$$

$$\dot{q} = \frac{M - F_{r_3}(x_{\mathrm{CG}} - x_{\mathrm{PA}}) - F_{r_1}(z_{\mathrm{CG}} - z_{\mathrm{PA}}) + (I_z - I_x)rp - I_{xz}(p^2 - r^2)}{I_y}$$

$$\dot{r} = \frac{I_{xz}\left[L + F_{r_2}(z_{\mathrm{CG}} - z_{\mathrm{PA}}) + L_b\right] + I_x\left[N + F_{r_2}(x_{\mathrm{CG}} - x_{\mathrm{PA}}) + N_b\right]}{I_x I_z - I_{xz}^2} + \frac{\left(I_x^2 - I_x I_y + I_{xz}^2\right)pq - I_{xz}(I_x - I_y + I_z)rq}{I_x I_z - I_{xz}^2} \tag{3}$$

where m is the mass of the capsule and I_x, I_y, I_z, and I_{xz} are the moments of inertia computed for the different c.g. locations.

The equations of motion for the parachute[9,10] with respect to the body axes x_P, y_P, and z_P are different from the conventional rigid-body case because the inertial terms include the contribution of added masses:

$$\dot{u}_P = \frac{X_P + F_{r_{1_P}} - (m_P + m_{ay})q_P w_P + (m_P + m_{ay})v_P r_P}{m_P + m_{ax}} - \frac{m_P g \sin\theta_P}{m_P + m_{ax}}$$

$$\dot{v}_P = \frac{Y_P + F_{r_{2_P}} - (m_P + m_{ax})r_P u_P + (m_P + m_{ay})p_P w_P + m_P g \cos\theta_P \sin\phi_P}{m_P + m_{ay}}$$

$$\dot{w}_P = \frac{Z_P + F_{r_{3_P}} - (m_P + m_{ay})p_P v_P + (m_P + m_{ax})q_P u_P}{m_P + m_{ay}} + \frac{m_P g \cos\theta_P \cos\phi_P}{m_P + m_{ay}}$$

$$\dot{p}_P = \frac{L_P}{I_{x_P}}$$

$$\dot{q}_P = \frac{M_P + F_{r_{3_P}} l_s - (I_{x_P} - I_{y_P} - I_{ay})r_P p_P - (m_{ax} - m_{ay})u_P w_P}{I_{y_P} + I_{ay}}$$

$$\dot{r}_P = \frac{N_P - F_{r_{2_P}} l_s + (I_{x_P} - I_{y_P} - I_{ay})p_P q_P + (m_{ax} - m_{ay})u_P v_P}{I_{y_P} + I_{ay}} \tag{4}$$

where m_P is the mass of the parachute, I_{x_P}, I_{y_P}, and I_{z_P} are the mass moments of inertia of the parachute, m_{ax} and m_{ay} are the axial and transverse added masses, and I_{ay} is the added moment of inertia. The added masses are constant, but they are dependent on the direction of the acceleration. They are computed with the method adopted in Ref. 8, based on the use of multipliers of the mass of air included by the canopy scaled to match the effects of porosity. Note that, due to the symmetry of the canopy, the transverse added mass m_{ay} and inertia I_{ay} are not influenced by the selection of the direction of the lateral axis y_P. The term I_{xz_P} is dropped in the moment equations assuming that the body axes x_P, y_P, and z_P are also the principal axes of the parachute and that the center of parachute apparent mass is coincident with parachute center of mass (CP).

The aerodynamic loads are obtained considering that symmetry applies for the inflated canopy. The drag and the lift are estimated in the plane defined by the body axis x_P and the velocity vector $\boldsymbol{V}_P$. Their components X_P, Y_P, and Z_P are derived with a procedure similar to that one used for the capsule, in terms of total angle of attack and aerodynamic roll angle. The terms L_P, M_P, and N_P include the aerodynamic damping of the canopy estimated according to the analytical method described in Ref. 18.

The trajectory of the capsule, that is, the coordinates of the c.g. with respect to s, y, and h where flat Earth is assumed with no winds, is evaluated by means of conventional kinematic equations, which relate the velocity components u, v, and w and the Euler angles ϕ, θ, and ψ with the time derivatives of the coordinates s, y, and h:

$$\begin{aligned}\dot{s} &= -u\cos\psi\cos\theta - v(\cos\psi\sin\theta\sin\phi - \sin\psi\cos\phi) \\ &\quad - w(\cos\psi\sin\theta\cos\phi + \sin\psi\sin\phi) \\ \dot{y} &= u\sin\psi\cos\theta + v(\sin\psi\sin\theta\sin\phi + \cos\psi\cos\phi) \\ &\quad + w(\sin\psi\sin\theta\cos\phi - \cos\psi\sin\phi) \\ \dot{h} &= u\sin\theta - v\cos\theta\sin\phi - w\cos\theta\cos\phi\end{aligned} \tag{5}$$

Equivalent equations are also adopted for computing the trajectory of the center of mass of the decelerator, that is, the coordinates of CP with respect to s, y, and h). The coordinates for the point of confluence $P2$ are derived from the location of the CP:

$$\{s_{P2}, y_{P2}, h_{P2}\}^T = \{s_{\mathrm{CP}}, y_{\mathrm{CP}}, h_{\mathrm{CP}}\}^T + [T_{PV}]^{-1} \cdot \begin{Bmatrix} -l_s \\ 0 \\ 0 \end{Bmatrix} \tag{6}$$

The coordinates for the PA are computed from the location of the capsule c.g.:

$$\{s_{\mathrm{PA}}, y_{\mathrm{PA}}, h_{\mathrm{PA}}\}^T = \{s_{\mathrm{CG}}, y_{\mathrm{CG}}, h_{\mathrm{CG}}\}^T + [T_{BV}]^{-1} \cdot \begin{Bmatrix} x_{\mathrm{CG}} - x_{\mathrm{PA}} \\ 0 \\ z_{\mathrm{PA}} - z_{\mathrm{CG}} \end{Bmatrix} \tag{7}$$

As a consequence, the angular displacements χ and τ of the riser with respect to s, y, and h are derived:

$$\tan\chi = \frac{h_{P2} - h_{\mathrm{PA}}}{\sqrt{(s_{P2} - s_{\mathrm{PA}})^2 + (y_{P2} - y_{\mathrm{PA}})^2}} \tag{8}$$

$$\tan\tau = -\frac{y_{\mathrm{PA}} - y_{P2}}{s_{\mathrm{PA}} - s_{P2}} \tag{9}$$

From the location of PA and $P2$, the riser elongation ϵ and its elastic reaction F_r are also obtained:

$$\epsilon = \frac{\sqrt{(s_{P2} - s_{\mathrm{PA}})^2 + (y_{P2} - y_{\mathrm{PA}})^2 + (h_{P2} - h_{\mathrm{PA}})^2} - l_{r_0}}{l_{r_0}}$$

$$\epsilon > 0 \rightarrow F_r = K_r \cdot \epsilon, \qquad \epsilon < 0 \rightarrow F_r = 0 \tag{10}$$

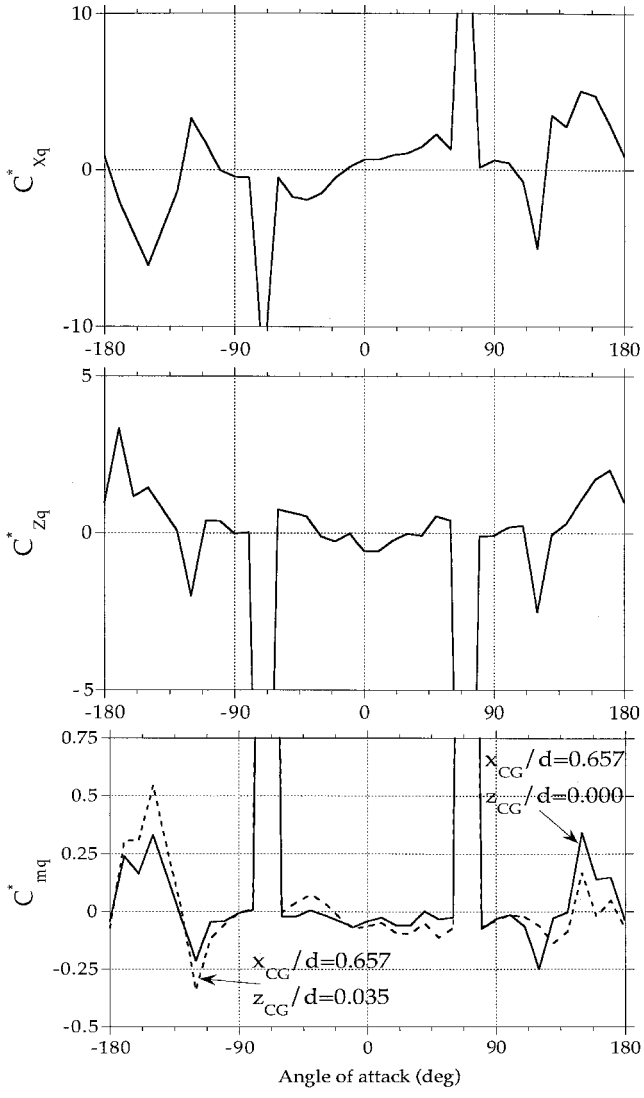

Fig. 3 Capsule damping derivatives, $V = 30$ m/s, $\Delta\theta = 5$ deg, and $\dot{\theta}d/V = 0.07$.

Note that the riser is treated as a linear hard-stop device because no elastic reaction is provided for $l_r < l_{r_0}$, where l_{r_0} is the length of the riser at rest. It is also assumed that no damping contribution is provided by the elongation of riser and bridles. The components of F_r acting along the body axes x_B, y_B, and z_B and x_P, y_P, and z_P are found:

$$\begin{Bmatrix} F_{r_1} \\ F_{r_2} \\ F_{r_3} \end{Bmatrix} = [T_{BV}] \cdot \begin{Bmatrix} -F_r \cos\chi \cos\tau \\ F_r \sin\chi \\ F_r \cos\chi \sin\tau \end{Bmatrix}$$

$$\begin{Bmatrix} F_{r_{1_P}} \\ F_{r_{2_P}} \\ F_{r_{3_P}} \end{Bmatrix} = [T_{PV}] \cdot \begin{Bmatrix} F_r \cos\chi \cos\tau \\ -F_r \sin\chi \\ -F_r \cos\chi \sin\tau \end{Bmatrix} \tag{11}$$

The Euler angles for the payload and the parachute can be replaced by quaternions, and the roll degree of freedom of the parachute can be also neglected. This last option is adopted for simulations, and friction in joints is not modeled.

The effects of atmospheric turbulence are optionally included in the present model. The linear velocity components u_g, v_g, and w_g and the angular velocity components p_g, q_g, and r_g are generated step-by-step according to the power spectra provided by the theoretical model developed in Refs. 19 and 20, including the variation of turbulence scale and standard deviation of components with aircraft altitude and airspeed. The gust components are subtracted from the velocity components of both payload and parachute.

Analysis of the Results

The data available from the reference flight tests[11,12] are used for the validation of the simulation of ARD terminal reentry dynamics.

The capsule is substantially a 70%-scaled version ($d = 2.8$ m) of the original ACM decelerated by a single conical ribbon drogue parachute (nominal diameter 5.8 m) inflated in two reefing stages and a cluster of three main polyconical slotted parachutes (nominal diameter 22.9 m) inflated in three reefing stages. The sequence of inflation and the parachute drag profile is time scheduled according to the planned reefing stages and inflation times.

The variation of capsule mass and parachute drag area with altitude is given in Table 1. The capsule moments of inertia and the location of the c.g. ($x_{CG}/d = 0.680 \div 0.698$ and $z_{CG}/d = 0.036 \div 0.039$) are also updated according to reference data during the simulation of the reentry phase. Note that the coordinates x_{CG} and z_{CG} of the capsule c.g. are measured along the auxiliary

Table 1 ARD terminal reentry phase (sequence of parachute deployment)

Sequence	Altitude, m	m, kg	m_P, kg	$C_{DP}S_P$, m^2
Mortar firing (pilot jettison)	13,996	2,651	——	——
Back cover separation	13,666	2,606	——	——
Drogue parachute snatch	13,430	2,587	19	14.5
Drogue parachute release	6,461	2,587	–	–
Main parachute snatch	6,364	2,475	112	976
Bridle cut (main parachute)	5,359	2,475	112	976

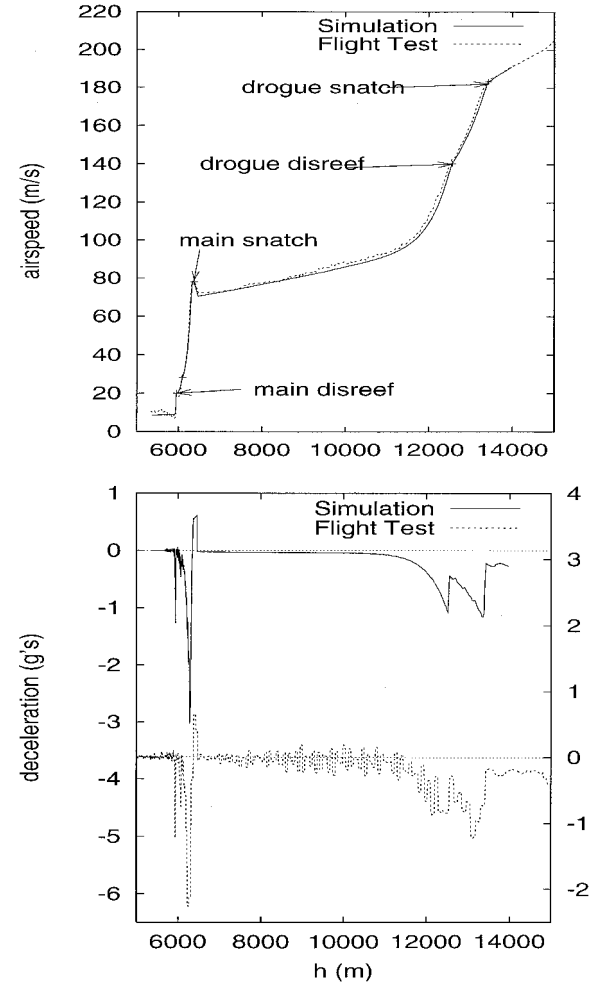

Fig. 4 Comparison of the time-domain results of simulation with flight-test data, complete parachute deployment sequence, mode A.

body-fixed longitudinal axes x and z with origin at capsule theoretical apex.

Flight-test atmospheric data are adopted to match the vertical gradient for air density and speed of sound. The components of wind are subtracted from flight-test data.

To validate the time and frequency domain response of the payload, three different reentry conditions were reproduced with simulations: 1) standard reentry program (mode A), 2) moderate intensity atmospheric turbulence where the standard deviation of linear velocity components is lower than 3 m/s (mode B) and 3) asymmetric bridles layout, that is, one of the bridles is assumed to be only partially stretched (mode C). A guess of 97.5% of the unstretched bridle length was adopted. These different reentry modes were investigated to verify the matching of simulations with experimental results under different flight conditions.

Parachute roll degree of freedom is neglected for the present analysis because the friction in joints is not modeled.

A comparison of velocity and deceleration profile with altitude is given in Fig. 4. Although the effects of compressibility are neglected for the interpolation of the aerodynamic database of the payload, the results of simulation substantially match the flight-test data. The moving average of the deceleration given by parachute reefing is also reproduced in terms of amplitude (gravitational acceleration) and time scheduling, even if the oscillatory nature of the flight data after parachute deployment is not captured. As a consequence of the large region of separation on the canopy, the real aerodynamic loads acting on the parachute are nonlinear with stochastic fluctuations. This behavior is filtered by the simulation model in which steady-state parachute aerodynamics is assumed. Another interesting point is that the deceleration peak due to the first reefing of the main parachutes is overpredicted. In the present mathematical model, clustered decelerators are treated as a single parachute with the same drag area with a single suspension system. Hence, an empirical correction for the aerodynamic interference of

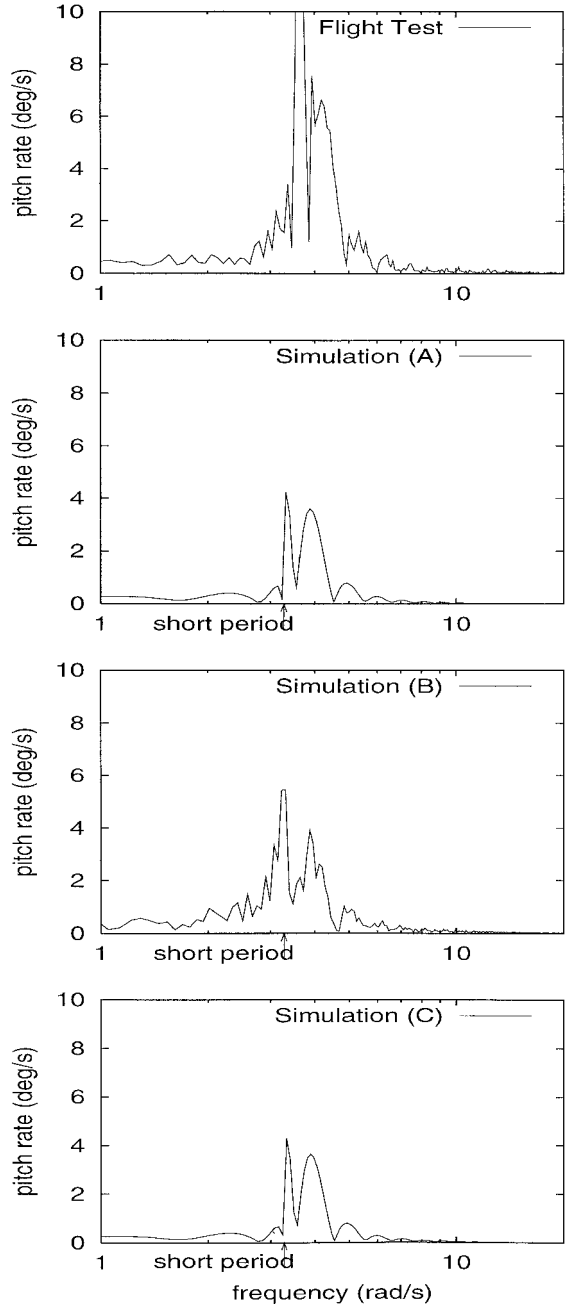

Fig. 5 Comparison of the pitch rate q frequency-domain results of simulation with flight-test data, drogue parachute deployment.

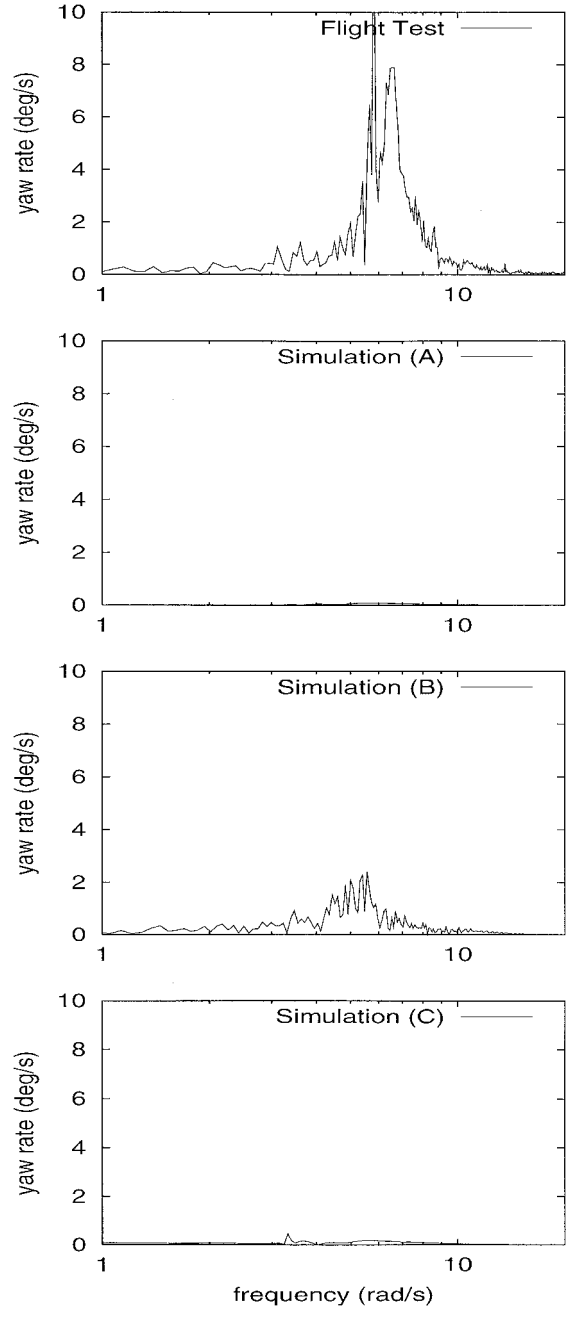

Fig. 6 Comparison of the yaw rate r frequency-domain results of simulation with flight-test data, drogue parachute deployment.

the parachutes should be included. The model for the suspension system should be also extended to reproduce the complexity of the real geometry.

The frequency-domain response for the payload angular rates during the drogue deployment phase is given in Figs. 5–7. Note that the longitudinal short period undamped natural frequency is also marked in Fig. 5. This frequency was obtained after numerical perturbation of the differential equations for capsule longitudinal dynamics.[17] The shape of pitch frequency response (Fig. 5) shows that capsule longitudinal dynamics is reproduced by the simulator, but the magnitude of the peaks is underpredicted. The comparison of simulations for the standard reentry mode A with flight-test data shows that yaw (Fig. 6) and roll (Fig. 7) rates are underpredicted unless at least the effects of severe atmospheric turbulence and large bridles asymmetry are included. As a matter of fact, the magnitude of longitudinal and lateral–directional responses observed during the ARD flight can be explained by external atmospheric perturbations (mode B) or by some unexpected misalignment in the suspension system of the decelerator (mode C). Atmospheric turbulence influences both payload and parachute aerodynamics that enhances the dynamic coupling of the two subsystems. Furthermore, the instantaneous change of capsule angle of attack due to gust components alters the payload dynamic stability as a consequence of the trend of the aerodynamic coefficients. Note that the effect of asymmetry is only affecting the lateral–directional degree of freedom by means of the torques L_b and N_b induced by the bridles. In particular, the divergence in roll (Fig. 7) may derive from significant asymmetric loading of bridles (mode C). The flight-test data also show an inertial coupling between the roll and the yaw degree of freedom that was probably triggered by the aforementioned roll divergence. Another source of discrepancy between flight-test data and simulations may be the accuracy in the location of the c.g. for the real ARD capsule during the reentry flight.

The same analysis is also performed for the main parachutes deployment phase (Figs. 8–10). This phase is characterized by a sharp

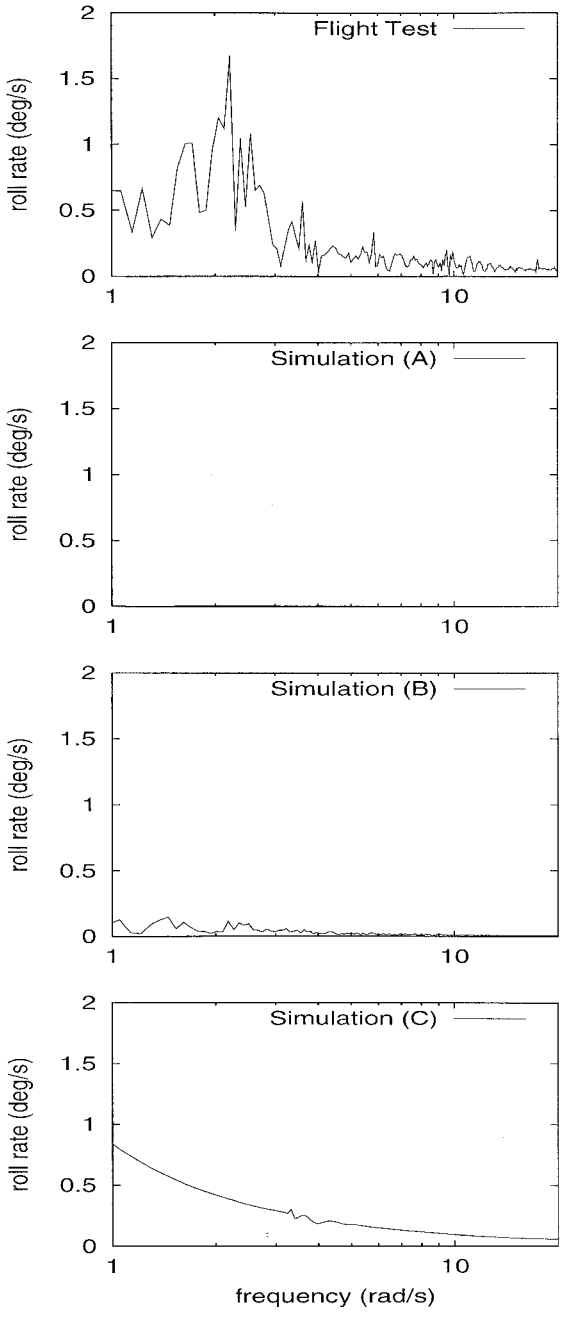

Fig. 7 Comparison of the roll rate p frequency-domain results of simulation with flight-test data, drogue parachute deployment.

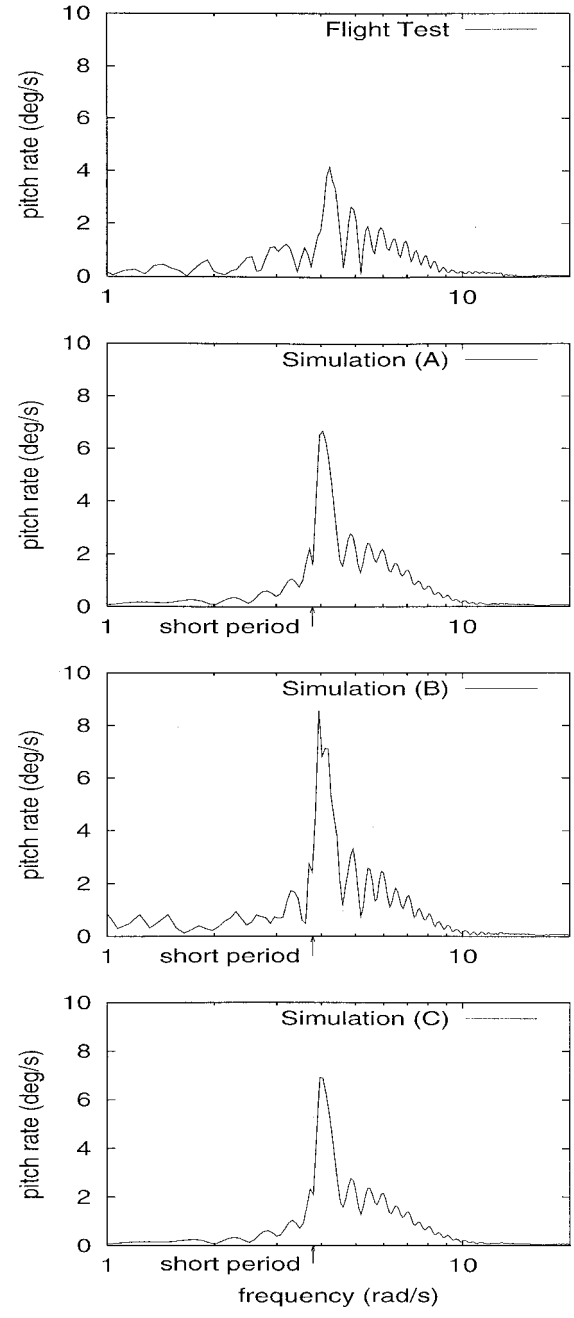

Fig. 8 Comparison of the pitch rate q frequency-domain results of simulation with flight-test data, main parachutes deployment.

decrease of dynamic pressure and a marginal contribution of capsule aerodynamics to the rotational equilibrium of the payload. Attitude dynamics is substantially driven by the decelerating forces generated on the parachutes, that is, by the torques L_b and N_b induced by the bridles. Different from the drogue deployment phase, the simulations for the main decelerators provide a better match with flight experimental results of pitch and yaw rate frequency response. The amplitude of pitch response (Fig. 8) is overpredicted due to larger deceleration given by the simulations for the first reefing stage of the main parachutes (Fig. 4). The geometry of the suspension system affects the shape of the frequency response for the yaw degree of freedom (Fig. 9) that predicts a peak in the lower frequency range not seen in flight-test data. Probably, the simplified model for the main parachutes suspension system is the reason for this mismatch. Roll dynamic response (Fig. 10) is underpredicted for the standard simulation conditions (mode A). The presence of perturbations provides a better match of in-flight data. However, the effect of external perturbations (mode B and C) on pitch and yaw attitude dynamics seems to be less significant in terms of matching with flight-test data.

The effect of capsule aerodynamic damping on pitch response is presented in Fig. 11. This analysis is intended to verify if the measurement accuracy of stability parameters C^*_{iq} can influence the validity of the results. The simulations (mode A) demonstrate that, even for the drogue deployment phase, where capsule aerodynamic derivatives are still strongly affecting the dynamic stability of the payload, significant changes of oscillation decay times are only obtained for large parametric changes of damping derivatives. These changes are at least one order of magnitude larger than the measurement accuracy of the experimental damping coefficients.[17]

The impact of some design parameters on capsule and parachute attitude dynamics is also evaluated to check if the mathematical model is able to reproduce the stability changes due to the coupling of the two subsystems. The dynamic stability of this kind of system is typically reduced for increasing riser length l_r and parachute

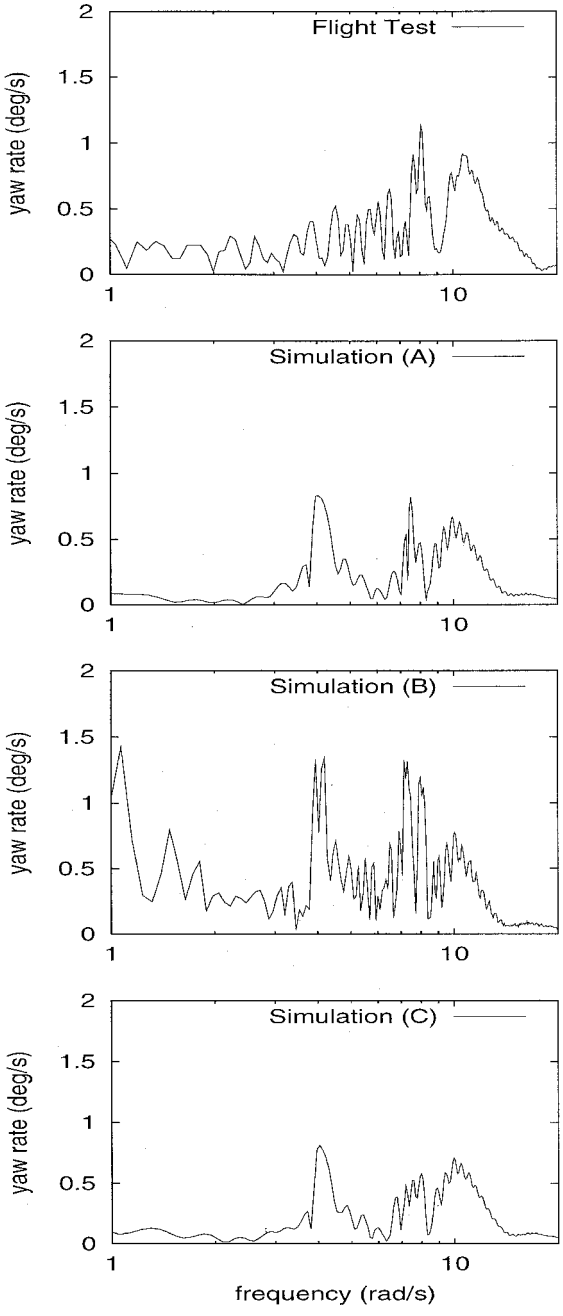

Fig. 9 Comparison of the yaw rate *r* frequency-domain results of simulation with flight-test data, main parachutes deployment.

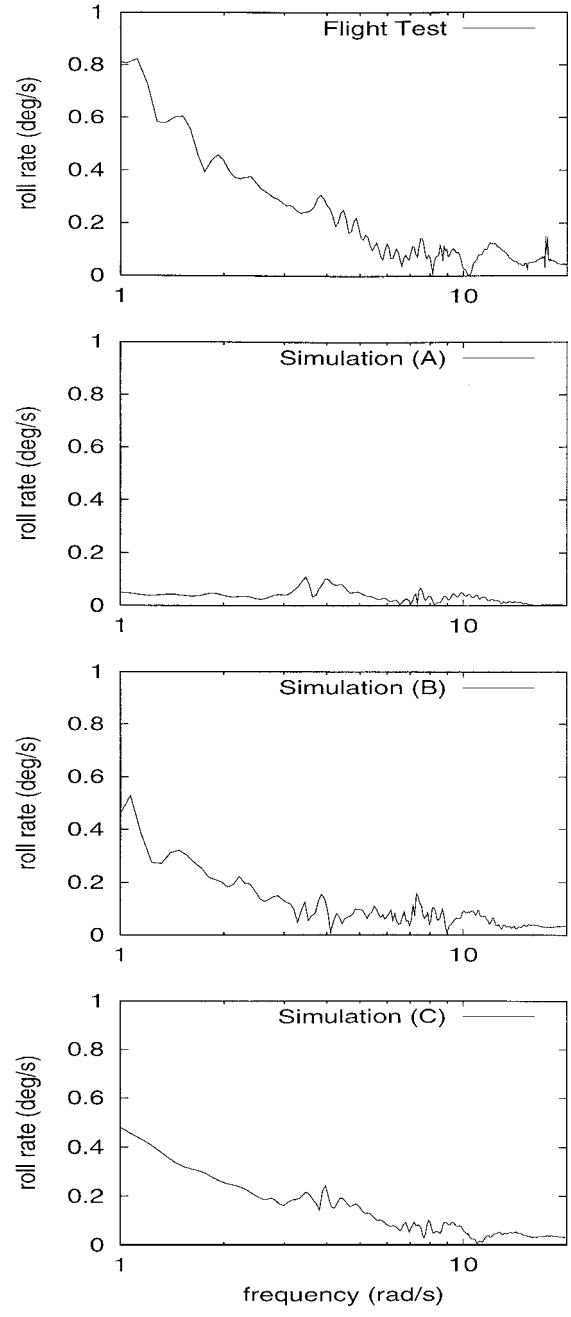

Fig. 10 Comparison of the roll rate *p* frequency-domain results of simulation with flight-test data, main parachutes deployment.

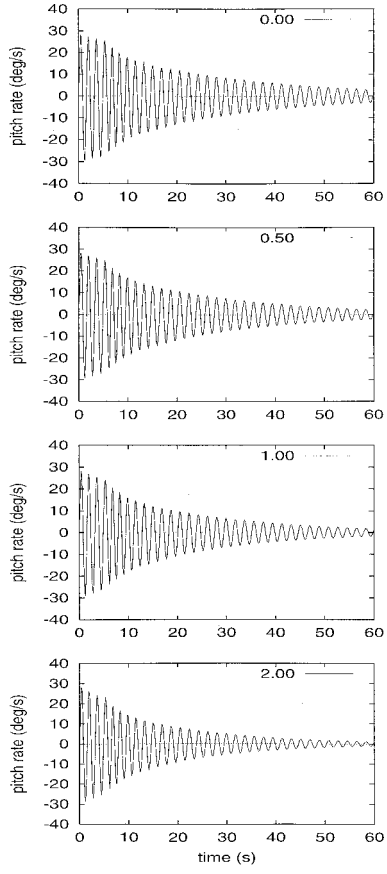

Fig. 11 Effect of aerodynamic damping ratio $C^*_{iq}/C^*_{iq_0}$ on the pitch rate q of the capsule, drogue parachute deployment, mode A.

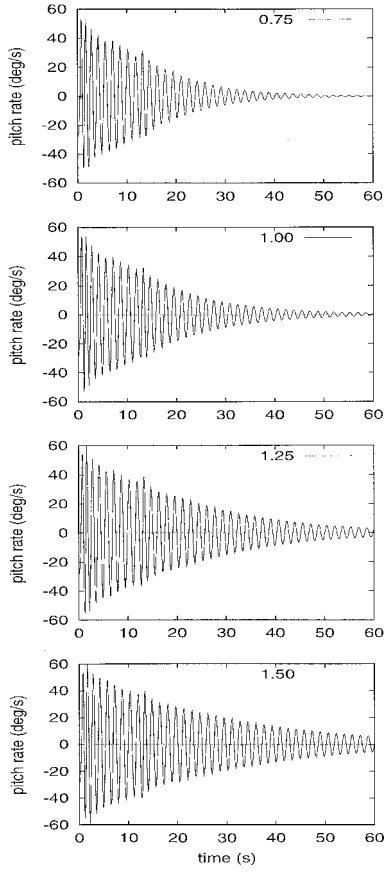

Fig. 12 Effect of riser length ratio l_r/l_{r_0} on the pitch rate q of the capsule, main parachutes deployment, mode A.

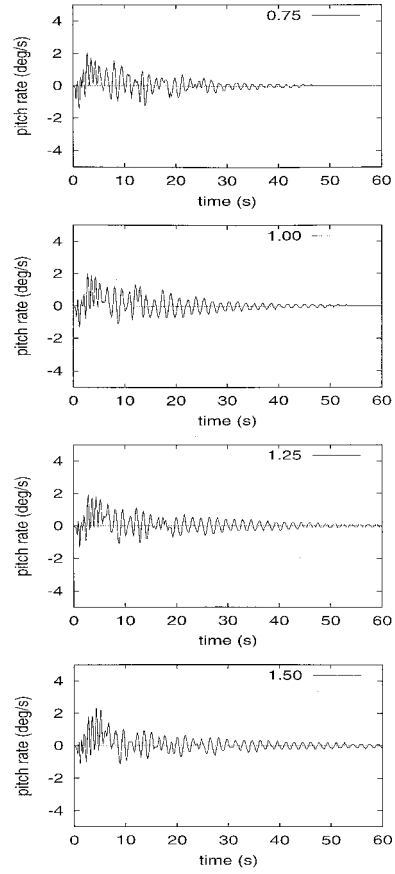

Fig. 13 Effect of riser length ratio l_r/l_{r_0} on the pitch rate q_P of the parachute, main parachutes deployment, mode A.

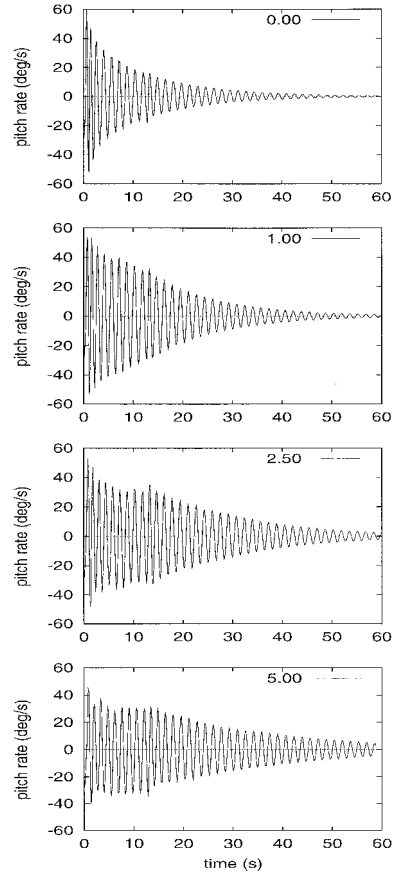

Fig. 14 Effect of parachute added mass ratio m_{ax}/m_{ax_0} on the pitch rate q of the capsule, main parachutes deployment, mode A.

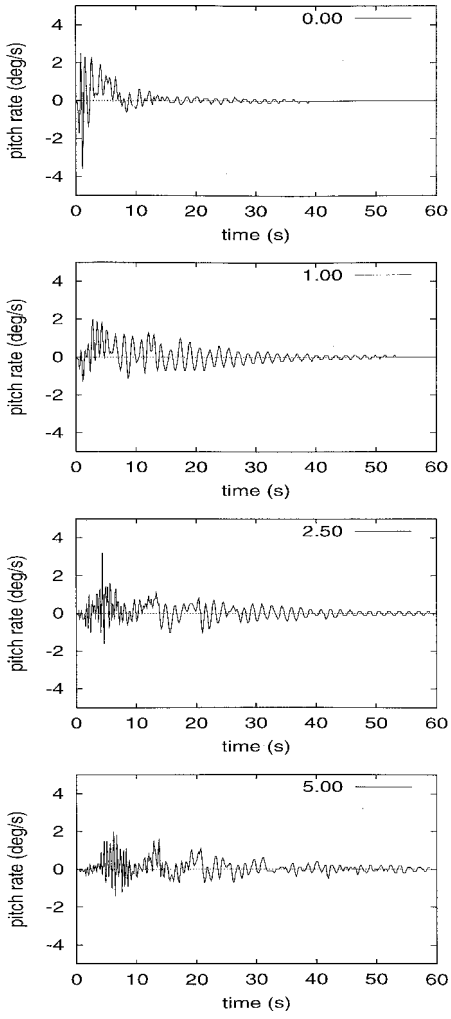

Fig. 15 Effect of parachute added mass ratio m_{ax}/m_{ax_0} on the pitch rate q_P of the parachute, main parachutes deployment, mode A.

added mass, as demonstrated by the detailed stability analysis performed in Ref. 6. This result is confirmed by the simulations (see Figs. 12–15). The results also show that, although the two subsystems are coupled in terms of frequency response, the motion of the parachute is generally limited in amplitude and highly damped. The relevant deceleration forces acting on the main parachutes reduce the oscillations induced on the canopy by payload dynamics. The assumptions adopted for the decelerator (rigid canopy, steady-state parachute aerodynamics and fixed length suspension system) introduce limitations in terms of simulation of the real oscillatory behavior of the parachute subsystem.

Conclusions

The experimental data set obtained at Politecnico di Torino for the ACM configuration was included in a mathematical model of payload-decelerator system. The system dynamic response obtained from simulations was compared with ARD flight-test data. The velocity profile and deceleration peaks given by parachute reefing were reproduced in terms of amplitude (gravitational acceleration) and time scheduling, although larger deceleration peaks are obtained for the main parachute reefing stages.

The frequency-domain attitude response of the capsule was simulated with acceptable fidelity during the main parachutes deployment. Discrepancies for the drogue opening phase were observed for lateral–directional response. Possible sources of inaccuracy are the effects of compressibility on capsule aerodynamic coefficients and the inaccurate estimation of c.g. The attitude response was also potentially affected by external factors (severe atmospheric turbulence) and/or large asymmetries in parachute suspension system.

The results suggest that several factors may increase the fidelity of simulations, such as correct modeling of suspension system geometry and flexibility, parachute aerodynamics, accuracy of payload inertial data, and accurate matching of real flight external perturbations.

The simulation model has also shown the ability to investigate the effect of design parameters on payload attitude dynamics.

The artificial increase of capsule damping coefficients produced observable effects on attitude time histories for large perturbations of the aerodynamic derivatives only. The dynamic stability of the system is also reduced for large increase of riser length l_r and parachute added mass.

The parametric analysis shows that the mathematical model is able to reproduce the coupling of payload attitude response with parachute dynamics. Nevertheless, the oscillation amplitude of the decelerator is always limited even for large angular displacements of the payload when large deceleration forces are acting on the parachutes.

Acknowledgments

The authors wish to thank Alenia Spazio (Turin, Italy) for providing the Atmospheric Reentry Demonstrator flight-test data and the Italian Space Agency for the financial support of the research activity.

References

[1]Baillion, M., "Blunt Bodies Dynamic Derivatives," Rept. R-808, AGARD, May 1997.

[2]Ericsson, L. E., and Reding, J. P., "Re-Entry Capsule Dynamics," *Journal of Spacecraft and Rockets*, Vol. 8, No. 6, 1971, pp. 579–586.

[3]Maydew, R. C., and Peterson, C. W., "Design and Testing of High Performance Parachutes," Rept. AG-319, AGARD, Nov. 1991.

[4]Neustadt, M., and Ericksen, R. E., Guiteras, J. J., and Larrivee, J. A., "Parachute Recovery System Dynamic Analysis," *Journal of Spacecraft and Rockets*, Vol. 4, No. 3, 1967, pp. 321–326.

[5]White, F. M., and Wolf, D. F., "A Theory of Three-Dimensional Parachute Dynamic Stability," *Journal of Aircraft*, Vol. 5, No. 1, 1968, pp. 86–92.

[6]Wolf, D. F., "Dynamic Stability of a Nonrigid Parachute and Payload System," *Journal of Aircraft*, Vol. 8, No. 8, 1971, pp. 603–609.

[7]Doherr, K. F., and Schilling, H., "Nine Degree-of-Freedom Simulation of Rotating Parachute Systems," *Journal of Aircraft*, Vol. 29, No. 5, 1992, pp. 774–781.

[8]Tory, C., and Ayres, R., "Computer Model of a Fully Deployed Parachute," *Journal of Aircraft*, Vol. 14, No. 7, 1977, pp. 675–679.

[9]Eaton, J. A., "Added Masses and the Dynamic Stability of Parachutes," *Journal of Aircraft*, Vol. 19, No. 5, 1982, pp. 414–416.

[10]Eaton, J. A., "Added Fluid Mass and the Equations of Motion of a Parachute," *Aeronautical Quarterly*, Vol. 34, No. 8, 1983, pp. 226–242.

[11]Portigliotti, S., Paulat, J. C., and Rives, J., "ARD Descent and Recovery Subsystem Dynamics and Trajectory Flight Data Evaluation," 1st Association Aeronautique et Astronautique de France, International Symposium on Atmospheric Reentry Vehicles and Systems, Arcachon, France, March 1999.

[12]Portigliotti, S., "Parachute Flight Dynamics Modeling and Simulation: Code Validation through ARD Post-Flight Analysis," 2nd Association Aeronautique et Astronautique de France, International Symposium on Atmospheric Reentry Vehicles and Systems, Arcachon, France, March 2001.

[13]De Giorgis, M., Borriello, G., Allasio, A., Vavala, R., Laveugle, T., and Cosentino, O., "Atmospheric Reentry Demonstrator Balloon Flight Test," *Journal of Spacecraft and Rockets*, Vol. 36, No. 4, 1999, pp. 507–510.

[14]Moseley, W. C., Moore, R. H., and Hughes, J. E., "Stability Characteristics of the Apollo Command Module," NASA TN-D-3890, 1967.

[15]Wang, F. Y., Karatekin, O., and Charbonnier, J. M., "Low Speed Aerodynamics of a Planetary Entry Capsule," *Journal of Spacecraft and Rockets*, Vol. 36, No. 5, 1999, pp. 659–667.

[16]Wang, F. Y., Charbonnier, J. M., Karatekin, O., and Paris, S., "Utilization of Low-Speed Experiments in Transonic Capsule Stability Research," *Journal of Spacecraft and Rockets*, Vol. 36, No. 5, 1999, pp. 774–776.

[17]Guglieri, G., and Quagliotti, F. B., "Low Speed Dynamic Tests on a Capsule Configuration," *Aerospace Science and Technology*, Vol. 4, No. 6, 2000, pp. 383–390.

[18]Cockrell, D. J., Eaton, J. A., and Morgan, C. J., "Longitudinal Oscillation Damping for Fully Inflated Parachute Canopies," AIAA Paper 79-0459, Jan. 1979.

[19]"Flying Qualities of Piloted Aircraft," MIL-HDBK-1797, Dec. 1997.

[20]Yeager, J. C., "Implementation and Testing of Turbulence Models for the F18-HARV Simulation," NASA CR-206937, 1998.